Vacuum 230 (2024) 113724

Contents lists available at ScienceDirect

Vacuum

journal homepage: www.elsevier.com/locate/vacuum

Enhancement of copper nanoparticle yield in magnetron sputter inert gas condensation by applying substrate bias voltage and its influence on thin film morphology

Florian Knabl[a], Dominik Gutnik[a,b], Prathamesh Patil[c], Christine Bandl[d], Tijmen Vermeij[b], Christian M. Pichler[c,e], Barbara Putz[a,b], Christian Mitterer[a,*]

[a] Department of Materials Science, Montanuniversität Leoben, Franz-Josef-Strasse 18, 8700, Leoben, Austria
[b] Laboratory for Mechanics of Materials and Nanostructures, Empa, Swiss Federal Laboratories for Materials Science and Technology, Feuerwerkerstrasse 39, 3602, Thun, Switzerland
[c] CEST Centre for Electrochemistry and Surface Technology GmbH, Viktor-Kaplan-Strasse 2, 2700, Wiener Neustadt, Austria
[d] Department of Polymer Engineering and Science, Montanuniversität Leoben, Franz-Josef-Strasse 18, 8700, Leoben, Austria
[e] Institute of Applied Physics, TU Wien, Wiedner Hauptstrasse 8-10, 1040, Wien, Austria

ARTICLE INFO

Handling Editor: Prof. L.G. Hultman

Keywords:
Magnetron sputter inert gas condensation
Nanoparticle synthesis
Low energy ion scattering spectroscopy
Thin film
Magnetron sputtering

ABSTRACT

Large-scale synthesis of high-purity nanoparticles is an intense topic of scientific research, with magnetron sputter inert gas condensation recognized as a promising, environmentally friendly technique avoiding wet chemical processes. This study explores the deposition of size-selected nanoparticles under varied substrate bias voltages and reports on a consequent increase in deposition rates up to 32 %. These alterations in substrate bias voltage induce a progressive change in the morphology of the resulting nanoparticle thin films, attributable to the increased kinetic energy of the nanoparticles. Comprehensive characterization via quadrupole mass spectroscopy of the nanoparticle flux, scanning electron microscopy, X-ray photoelectron spectroscopy, and low-energy ion scattering spectroscopy of the deposited nanoparticles corroborates the enhanced nanoparticle yield associated with increased substrate bias voltage. These findings signify a methodological advancement, enhancing the efficiency of magnetron sputter inert gas condensation and moving the technology a step further towards feasible industrial production.

1. Introduction

The exploration of nanoparticles (NPs) has become an integral part of materials science, with practical applications ranging from catalysis [1], photocatalysis [2], hydrogen sensing [3], hydrogen storage [4], functionalized textiles for oil-water separation [5] to antibacterial [6] and antiviral [7] surfaces. Such applications are possible as NPs exhibit distinct physical and chemical properties, which can significantly differ from their bulk counterparts due to their small size and thus high surface-to-volume ratio. This has led to an increased research focus on the controlled synthesis and characterization of NPs to better understand their synthesis-structure-property behavior.

Magnetron sputter inert gas condensation (MS-IGC) is a physical vapor deposition technique for NP synthesis, offering a pathway to generate high-purity particles via a dry process. Initially presented by Haberland et al., in 1991 [8], this method combines NP formation by inert gas condensation with enhanced deposition rates achieved by magnetron sputtering. Additionally, magnetron sputtering also supports the processing of refractory metals, including tungsten and molybdenum, unavailable with evaporation-based cluster sources. The process commences with the sputtering of atoms from a target material within an aggregation chamber, typically maintained at a pressure between 10 and 100 Pa. Still in the vapor phase, these atoms then undergo condensation, beginning with the formation of diatomic clusters through a three-body collision step involving an inert gas, often argon. As these nascent clusters migrate through the aggregation chamber, they

---

* Corresponding author.

E-mail addresses: florian.knabl@alumni.unileoben.ac.at (F. Knabl), dominik.gutnik@unileoben.ac.at (D. Gutnik), prathamesh.patil@cest.at (P. Patil), christine.bandl@unileoben.ac.at (C. Bandl), tijmen.vermeij@empa.ch (T. Vermeij), christian.pichler@cest.at (C.M. Pichler), barbara.putz@unileoben.ac.at (B. Putz), christian.mitterer@unileoben.ac.at (C. Mitterer).

https://doi.org/10.1016/j.vacuum.2024.113724
Received 25 July 2024; Received in revised form 10 October 2024; Accepted 10 October 2024

accumulate additional atoms, leading to progressive growth. Upon entering a differentially pumped high-vacuum chamber, the growth of these NPs is considered to stop and a beam of NPs with a sharp size distribution is obtained. The NPs comprise a mixture of positively charged, negatively charged, and neutral particles, with their individual fractions being according to literature largely different [9–11]. The dominant NP fraction carries a single charge [12], making them susceptible to electrostatic manipulation. For instance, insertion of a biased grid enables to measure an electrical current, which allows to determine the NP flux in-situ [13]. For the Cu NPs addressed in this work, we know from an earlier study that the predominant contributions originate from negatively charged nanoparticles [13]. This allows the selection of NPs based on their mass-to-charge ratio, utilizing either time-of-flight or quadrupole mass spectrometry (QMS). Specifically, a quadrupole mass filter can be employed to isolate NPs of a desired mass — and by inference, assuming a known crystal density and spherical geometry, a specific size — resulting in a refined size distribution. At the time of writing, MS-IGC did not yet achieve a commercial breakthrough and a subsequent large-scale application in industry, in particular due to a still insufficient deposition rate [14].

Advancements in the MS-IGC technique have focused on enhancing the efficiency and stability of NP synthesis. Notably, the introduction of trace amounts of reactive gases such as O_2 [15], H_2/CH_4 [16], and water vapor [14] into the inert gas stream has shown promise in increasing the yield and process stability. From an engineering point of view, the development of a full-face erosion magnetron [14] aims to optimize target material utilization, addressing the prevalent issue of a decreasing deposition rate associated with race track formation during sputtering [17] and optimization of the gas flow within the aggregation chamber through computational fluid dynamics models can reduce NP losses to chamber walls [18]. Separately, in his early work MS-IGC pioneer Haberland already applied a substrate bias voltage to accelerate metallic NPs towards the substrate [8,19]. This was later-on studied by various authors, reporting smoothening or roughening phenomena of initially rough or smooth surfaces, respectively [20], flattening of individual nanoparticles with increasing bias voltage [21] or the formation of thin film structures with varying degrees of porosity [22]. These works identify three principal deposition regimes for nanoparticles, namely soft landing, pinning, and implantation, which are distinguished by their respective kinetic energy per atom [23]. However, none of the authors discussed if applying a substrate bias voltage could increase the NP deposition rate and thus the efficiency of the process.

In this study we demonstrate for the first time how the application of a substrate bias voltage enhances the extraction of NPs up to 32 % from a source operating with the MS-IGC principle, by monitoring both the in-situ QMS signal of the entire nanoparticle flux and the amount and morphology of nanoparticles arriving on the substrate, as visualized in Fig. 1. Two different NP sizes, namely 8 nm and 1.8 nm, are studied in detail, to investigate the influence of particle energy and landing condition. The resulting NP thin films are characterized by scanning electron microscopy (SEM), as well as X-ray photoelectron (XPS) and low-energy ion scattering spectroscopy (LEIS). Our findings indicate that applying a substrate bias voltage does allow to extract an increased quantity of NPs out of the NP source, while simultaneously affecting the morphology of the thin film formed by NP deposition.

2. Materials & methods

2.1. Materials

Cu NPs were produced by magnetron sputter inert gas condensation using Cu targets supplied by Kurt J. Lesker Company Ltd, with a purity of 99.999 %, a diameter of 25.4 mm, and a thickness of 3.2 mm. Cut single-crystal Si (100) wafers with a thickness of 525 μm (MicroChemicals GmbH) were employed as substrates.

To ensure a clean substrate surface for the deposition of NPs, a two-step cleaning process was implemented. Initially, samples were ultrasonically cleaned for 10 min in an isopropanol bath and subsequently dried using hot air. The substrates were then exposed to a low-pressure plasma environment using a Tetra 30 plasma system by Diener electronic GmbH & Co KG. During this stage, an Ar gas flow was maintained at 80 sccm, and the plasma was generated at 20 % of the system's full

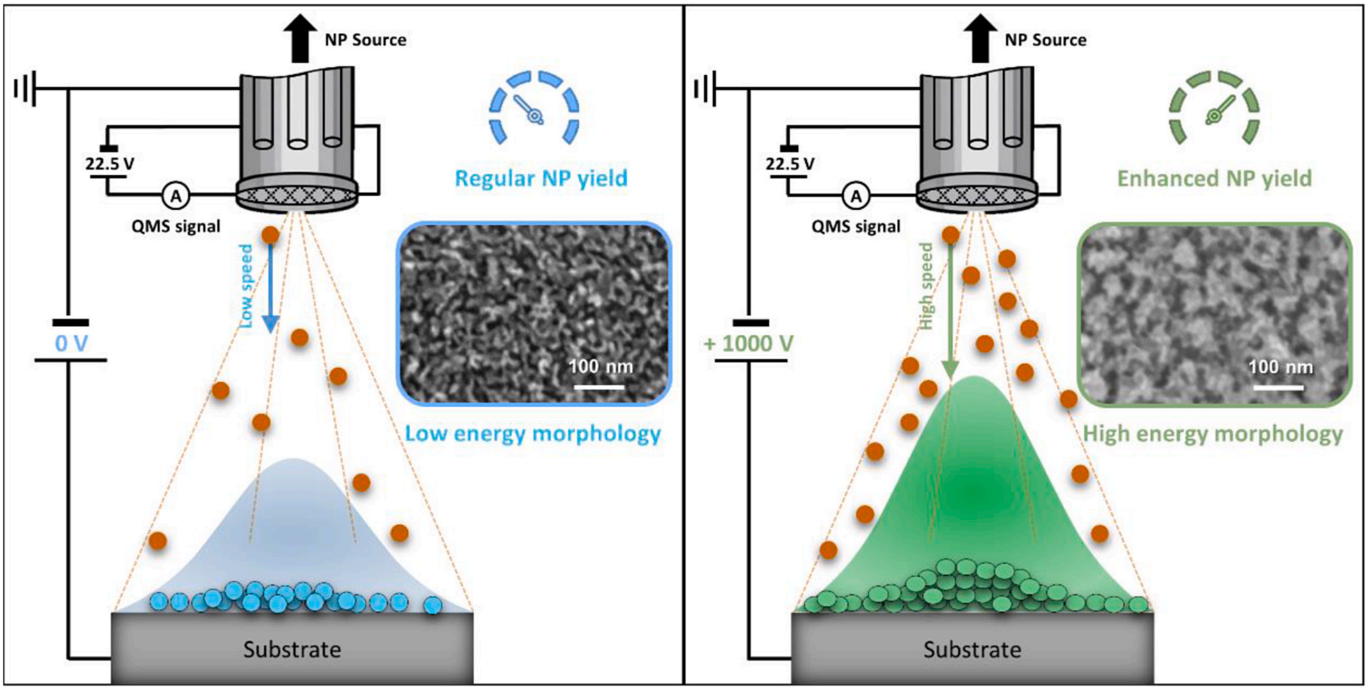

Fig. 1. Synthesis schematic of Cu nanoparticles using the magnetron sputter inert gas condensation (MS-IGC) principle; substrate bias voltages between 0 and 1000 V are used in this work. When the substrate bias is applied, we detect an increase in the NP flux (expressed by an increase in the QMS signal), enhancing the NP yield of the fabrication process. The additional kinetic energies of impinging NPs markedly influence the NP-surface interaction and resulting thin film morphology.

power capacity of 1 kW for a duration of 10 min, effectively removing any remaining contaminants and preparing the substrate surface for NP deposition.

2.2. Nanoparticle synthesis

Cu NPs were synthesized using an NL NL-DX3 nanoparticle deposition source (Nikalyte Ltd) attached to a MiniLab 125 deposition system (Moorfield Nanotechnology Ltd), with an extensive description of the system available in an earlier work [13]. NP nucleation and growth occurs within an aggregation chamber containing three individual metal targets, where only one Cu target was sputtered within this work. The length of the aggregation chamber, which we define as the distance between the metal targets and the 3 mm orifice terminating the aggregation chamber, can be tuned using a linear translator, thus influencing the NP growth conditions within the chamber. After terminating the aggregation chamber, the NPs arrive in a differentially pumped expansion zone, and further growth is assumed to stop. NPs leaving the aggregation chamber are assumed to be fully developed, roughly spherical, carrying mostly a single electric charge. In the subsequent expansion zone, a QMS is situated. With the assumptions of a spherical nanoparticle shape, a single electric charge, and a crystal density equivalent to that of bulk copper (9.0 cm^3 g^{-1}), the NP size distribution can be calculated. The NP flux is measured using the current detected at a grid located at the exit of the QMS. As outlined in an earlier study, the recorded data can be used to calculate the mass flux and the total deposited NP mass [13].

Substrates were mounted on the sample holder and subjected to a constant rotation speed of 10 rpm during deposition to ensure uniform coverage, without the application of external heating. The deposition processes were conducted under a base pressure below 5×10^{-5} Pa, with operational pressures reaching 0.17 Pa for 8 nm NPs and 0.13 Pa for 1.8 nm NPs within the deposition chamber.

For the 8 nm size-selected NPs, deposition parameters were set to a 30 min duration, an Ar gas flow rate of 70 sccm, an aggregation length of 90 mm, and a sputter current of 200 mA. For 1.8 nm size-selected NPs, an Ar flow of 40 sccm, an aggregation length of 60 mm, and a sputter current of 200 mA was used for a total deposition time of 45 min. Deposition parameters were chosen to achieve robust QMS grid current signals, as detailed in Section 3.1. For all samples, the same target was utilized to maintain consistency across all samples.

Prior and after deposition, the quadrupole mass spectrometer was used to determine the NP size distribution, operating in positive grid bias mode. Throughout the deposition process, nanoparticles were filtered by size (specifically 8 or 1.8 nm, equivalent to 1.44×10^6 amu and 1.64×10^4 amu, respectively) and continuously monitored throughout the deposition using the quadrupole mass spectrometer. The chosen positive substrate bias voltage (0 V, 300 V, 1000 V) was applied, then the substrate shutter was opened, resulting in a distinct step in the detected grid current. NP size distributions were recorded with a closed shutter and at 0 V for all samples, to ensure comparable measurement conditions and to allow for direct comparison of the deposition process without taking the effect of the substrate bias voltage into account.

2.3. Characterization methods

SEM micrographs were recorded using a Hitachi S4800 scanning electron microscope. All micrographs were recorded using a secondary electron detector for surface topology with an acceleration voltage of 3 kV. Focused ion beam (FIB) cross-sections and corresponding SEM micrographs to estimate the NP thin film thickness were made in a Tescan Lyra3. The NP thin film was protected by electron and ion beam deposited Pt layers. Cross-sectional FIB milling was conducted by stepwise reduction of the ion current from 2 nA to around 25 pA. The corresponding film thicknesses were measured by tilting of the sample and using the built-in tilt correction.

Image analysis of SEM micrographs for assessing the morphological development was performed in ImageJ. For this purpose, a Gaussian blur filter was used to reduce noise in the micrographs. Three greyscale thresholds were used to distinguish and quantify unfilled portions or groves of the NP films. Trends in the development of mean size and total number of formed NP agglomerates and the relative unfilled area were evaluated for all depositions.

The XPS measurements were carried out using a Thermo Scientific Nexsa G2 X-ray photoelectron spectrometer system, following the experimental protocol outlined by Greczynski and Hultman [24]. The base pressure during spectra acquisition was below 3×10^{-7} mbar, maintained by an Edwards nXDS6i pump. No residual gas analysis was performed. An Al Kα anode (1486.7 eV) served as the excitation source, and a monochromator was used. Wide-scan XPS spectra were recorded with a pass energy of 100.0 eV and a step size of 1.0 eV, while high-resolution spectra were acquired with a pass energy of 20.0 eV and a step size of 0.1 eV. Both types of spectra were recorded over a spot size of 300 μm in sequential mode with a total acquisition time of 12 h per sample. The calibration and linearity of the binding energy scale was confirmed by referencing standard core-level photoelectron peaks of Au $4f_{7/2}$, Ag $3d_{5/2}$, and Cu $2p_{3/2}$. With the selected parameters, the energy resolution was determined by measuring the Full Width at Half Maximum (FWHM) of the Ag $3d_{5/2}$ peak using a standardized procedure. This procedure automatically acquired Ag 3d spectra at X-ray spot sizes of 400, 200, 100, 50, and 30 μm, using a pass energy of 90 eV (80 eV for the 400 μm spot). Under these conditions, the Ag 3d FWHM was proven to be ≤ 1 eV. The system automatically moved to the silver standard sample, sputtered it at 1 keV for 20 s, and then acquired spectra, measuring the FWHM and intensity above a linear background from binding energies of 365 eV–371 eV with 1 eV background averaging. Additionally, a spectrum was acquired at a low pass energy of 3 eV to demonstrate an ultimate energy resolution of ≤ 0.5 eV. The analyzed sample area consisted of a rectangular grid measuring 1.5 mm × 21 mm, with 0.5 mm spacing between points. No complementary ultraviolet photoelectron spectroscopy (UPS) was performed to determine the sample work function [25]. The 8 nm samples were stored for 1 week, and the 1.8 nm samples for 5 weeks, in an air-tight sample storage box made of acrylonitrile butadiene styrene and polystyrene under standard office conditions before XPS analysis. No sputter cleaning, baking, or capping layer was applied to the samples. To mitigate charging effects, all spectra were referenced to the C1s peak at 284.8 eV (sp^2 hybridized carbon). Due to the absence of UPS data, we did not apply more accurate, state-of-the-art binding energy referencing methods [24,26,27], and thus cannot definitively assign specific chemical states to elements. However, this approach is sufficient for determining the Cu NP loading on Si surfaces.

The LEIS spectra were obtained using an ionTOF Qtac100 spectrometer, employing He ions as the probing species with an energy of 3 keV. The primary ion beam was directed at the sample surface with a perpendicular incidence angle, and scattered ions were detected at a scattering angle of 145°. Prior to each measurement, the samples were cleaned in-situ by sputtering with an Ar ion beam of 1 keV for 25 s. A time of flight filter was used to reduce the background signal from lighter elements.

3. Results & discussion

3.1. Nanoparticle synthesis

As shown in Fig. 2, an increase in the positive bias voltage (300 V and 1000 V) applied to the substrate during NP deposition causes a corresponding rise in the QMS grid current, which serves as an indicator of the NP flux within the system [13] and thus implies an increase in extracted NPs. This effect was consistently evident across the overall NP size distribution, as demonstrated in Fig. 2a, as well as in the QMS grid current signal obtained when monitoring a specifically filtered NP size during deposition, as shown in Fig. 2b.

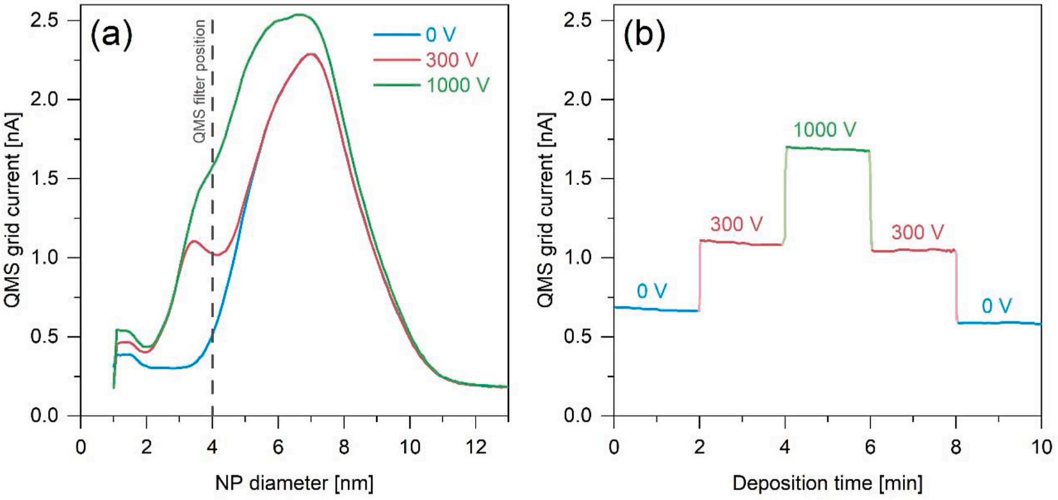

Fig. 2. In-situ QMS data revealing an apparent increase in NP flux with applied substrate bias voltage. This increase is visible in the (a) NP size distribution as determined by the QMS and the (b) time-resolved QMS grid current for a selected NP size (e.g. 4 nm, filter position indicated in a) by dashed line), with increases corresponding to the application of 300 V and 1000 V bias voltage, illustrating the reversible nature of the substrate bias voltage effect on the NP flux.

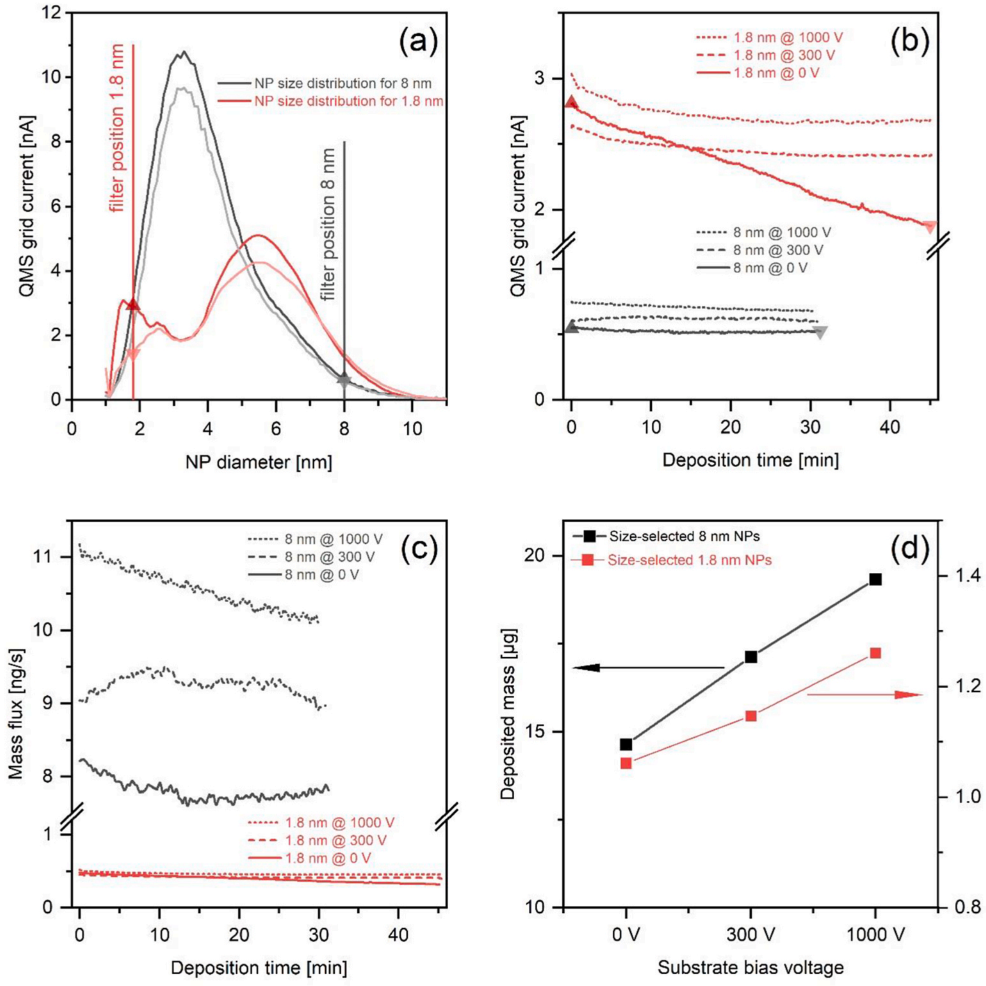

Fig. 3. In-situ QMS analysis of NP deposition dynamics. (a) Size distribution of NPs before (darker shade) and after (lighter shade) deposition. Filter positions are indicated by vertical lines. (b) Temporal evolution of QMS grid current, indicative of the NP flux during deposition. Both in panels (a) and (b) up-pointing (▲) and down-pointing (▼) triangles indicate the QMS grid current at the beginning and end of the deposition time. (c) Temporal evolution of the calculated mass flux, showing the impact of the substrate bias voltage on the deposition rates for NPs of both sizes. (d) Relationship between applied substrate bias voltage and the resulting NP deposition mass, taking the deposition time into account.

A possible interpretation could be that the variation in the response of different NP sizes is due to their differential susceptibility to electrostatic forces. According to Newton's Second Law of Motion ($F = m \times a$), for a constant electrostatic force F applied to charged particles, smaller NPs experience greater acceleration a due to their lower mass m. This explains why lower bias voltages, such as 300 V, are effective at influencing smaller NPs (1–4 nm), while larger NPs (up to 8 nm), with greater mass, require a higher voltage (1000 V) to achieve a similar effect. Consequently, the size-dependent behavior observed in the QMS grid current might reflect the varying degrees of acceleration imparted on NPs of different sizes by the same electrostatic force.

Substrate bias variation to enhance the NP yield was performed for two different nanoparticle sizes: 8 nm and 1.8 nm diameter. Fig. 3a shows representative NP size distributions, measured before and after deposition (dark/lighter shade, respectively, 0 V bias), which exhibit either a Gaussian or a bimodal Gaussian shape, depending on the deposition parameters. These distributions were selected for our experiments, given that they yielded robust QMS grid current signals (indicative of the NP flux in NPs s^{-1}) for our targeted NP sizes of 8 and 1.8 nm. The filter positions are indicated with vertical lines in Fig. 3a and the corresponding QMS grid currents recorded at the start and end of the depositions are marked by up-pointing (▲) and down-pointing (▼) triangles, respectively. We opted not to select the peaks from the NP size distributions in favor of achieving a more substantial difference in NP mass. By comparing NP size distributions before and after deposition, we confirmed that the process maintained a comparable NP size range consistently across all experiments.

During deposition, the QMS was operated in filter mode, allowing only size-selected NPs of either 8 nm or 1.8 nm to deposit on the substrate and the QMS grid current was monitored to assess the size-specific NP flux, as shown in Fig. 3b. Notably, the 1.8 nm NPs without substrate bias experienced a significant 50.7 % reduction in deposition rate over the 45 min time, the most substantial change observed within the investigated time-period. Depositions at 300 V and 1000 V for 1.8 nm NPs showed similar, albeit less dramatic, decreases, aligning with documented behavior in MS-IGC literature [10,15,17,28–30]. This pronounced effect at 0 V for 1.8 nm NPs is likely due to the shorter aggregation length used in their synthesis, rendering the MS-IGC process more sensitive to subtle variations, such as the progressing target erosion over sputtering time. The 8 nm samples display a significantly lower absolute grid current and thus NP flux. This is, however, offset by the difference in mass with an 8 nm NP possessing approximately 90 times more mass than a 1.8 nm NP. As depicted in Fig. 3b, the QMS results indicate that an elevated substrate bias voltage leads to an increase in the grid current signal for 8 nm NPs as well, implying a greater deposition rate of NPs.

In Fig. 3c, the QMS grid current, which reflects the nanoparticle flux in NPs s^{-1}, is converted into the corresponding mass flux in ng s^{-1} [13]. Due to the significant mass disparity between 8 nm and 1.8 nm NPs, fewer 8 nm NPs can generate a substantially greater mass flux. This is because the mass flux $\dot{m}$ is obtained by multiplying the NP's mass m by its flux, the latter being directly proportional to the QMS grid current I_{QMS}, thus $\dot{m} \propto I_{QMS} \times m$.

With increasing substrate bias voltage, there is an anticipated rise in the mass of deposited 8 nm NPs. While two of the three recorded curves adhere to the commonly observed trend of decreasing NP flux throughout the deposition process, the curve at 300 V deviates, exhibiting a slight uptick in deposition rate over time — rising from 9.0 to 9.5 ng s^{-1} and then approximating the initial value after a 30 min deposition period. The observed phenomenon can be attributed to two competing effects; firstly, a reduction in the deposition rate originating from a decrease in oxygen impurities in the aggregation chamber [10]; and secondly, a gradual shift in the NP size distribution towards larger mean sizes, a consequence of ongoing race track formation [17]. Integration of the data from Fig. 3c yields the total deposited mass, as illustrated in Fig. 3d. Consistent with the earlier observations, these results emphasize that the deposited mass increases with higher substrate bias voltage for both NP sizes, with the largest increase observed for the 8 nm samples, where a 32 % rise in deposited mass was calculated.

3.2. *Nanoparticle thin film morphology*

SEM micrographs captured near the NP beam center (position indicated in Fig. 5d), where NP loading reaches its maximum, are presented in Fig. 4, for both NP sizes. These images indicate a more pronounced coverage with NPs with higher substrate bias voltage, thus indicating enhanced material deposition and thin film thickness. The film thickness of our sample series ranges from 10 nm for the 1.8 nm NP samples to 40 nm for the 8 nm NP samples, as determined in the vicinity of the NP beam center by cross-sectional FIB analysis. Additionally, the morphology undergoes a notable transformation with increasing substrate bias voltage. Specifically, size-selected 8 nm NPs (Fig. 4a, c, e) transition from a semi-dense distribution to larger agglomerates as the substrate bias voltage increases, leading to less pronounced surface features and fewer open channels separating the agglomerates. At 1000 V, the thin film becomes denser with larger agglomerates and a reduction of channels. It should be noted that the NP sizes visible in the SEM micrographs are larger than the NP sizes determined via QMS due to particle agglomeration, which shifts the average apparent particle size in SEM to larger values. Therefore, a direct comparison between SEM micrographs (representing post-deposition agglomerated particles) and QMS data (representing in-flight individual NPs) is not possible. In summary, the application of a substrate bias voltage not only increases NP loading but also induces significant morphological changes, resulting in a denser thin film.

For the 1.8 nm size-selected NP thin films, a uniform distribution of finely dispersed NPs characterizes the morphology at 0 V (see Fig. 4b, d, f). As the substrate bias voltage increases, a higher NP loading is evident, where the surface of the formed thin film transitions from small, finely distributed agglomerates to slightly larger, possibly patterned morphologies. At 1000 V, the morphology markedly shifts to even larger agglomerates, separated by clearly defined channels. In conclusion, increasing the substrate bias voltage enhances NP loading and promotes the coarsening of the surface topography.

Image analysis of the presented high-resolution SEM micrographs was conducted to assess the prevalence of channels or pores on the sample surface, showing a decrease in the area attributed to channels or pores with increasing substrate bias voltage for both NP sizes.

An examination of the morphological evolution from the center of the NP beam outward reveals a notable decrease in NP loading. This observation is in agreement with subsequent findings from XPS and LEIS investigations, detailed in the following paragraphs, and an earlier study by our group [13].

3.3. *Nanoparticle coverage*

To quantify NP deposition, XPS analysis was conducted, investigating the surface chemical composition within the topmost 5–10 nm layer of the deposited NP thin films. Fig. 5a summarizes representative wide-scan XPS spectra near the beam center, confirming the presence of Si, C, O, and Cu elements. Notably, the Cu peak intensity demonstrates a positive correlation with substrate bias voltage, suggesting an increased Cu accumulation at higher substrate bias voltages. This trend is confirmed by the high-resolution Cu spectra shown in Fig. 5b, which indicate a progressive rise in Cu content for both NP diameters as the substrate bias voltage is increased. In contrast, high-resolution Si scans reveal only minor Si signals, which diminish as the substrate bias voltage increases.

Due to inherent difficulties in performing an accurate peak fitting of Cu 2p photoemission spectra [31], we performed peak fitting on the O 1s spectra (Fig. 5c). This revealed contributions from both organic carbon-oxygen bonds most likely associated with adventitious carbon as

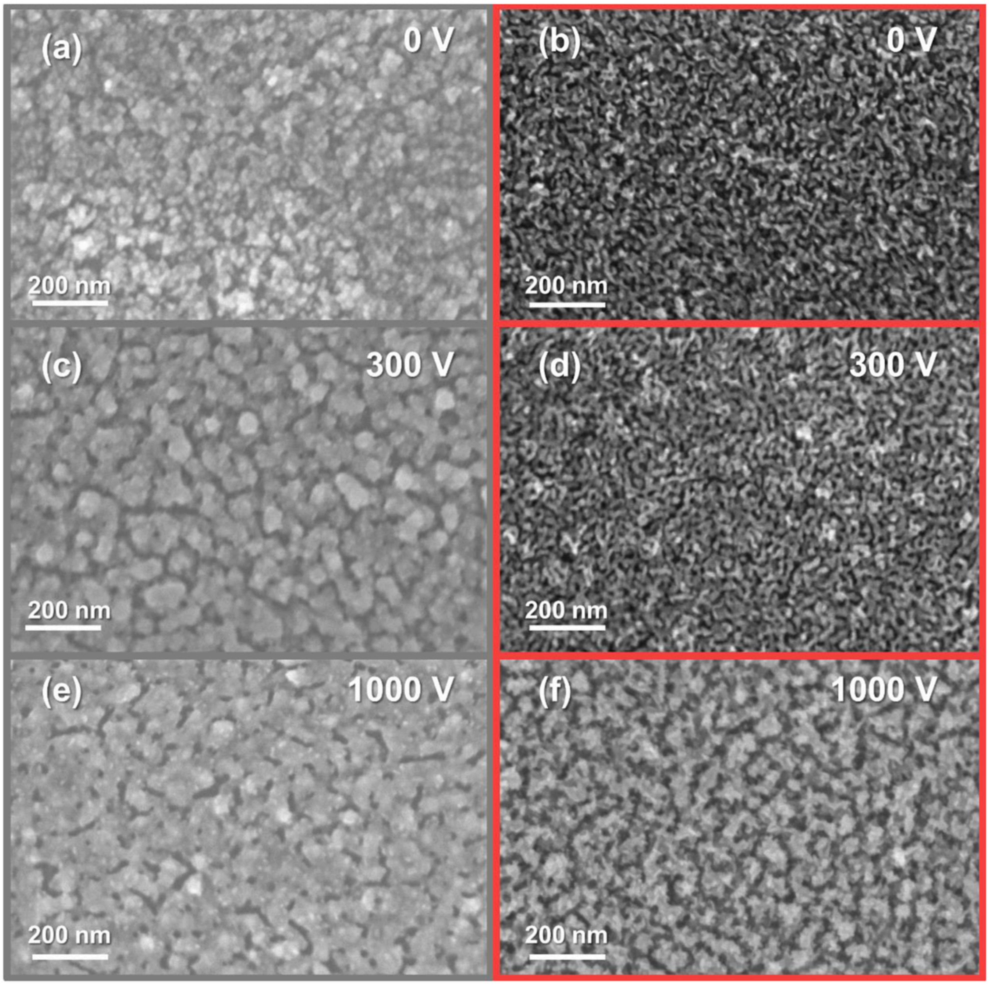

Fig. 4. SEM micrographs of thin films created from size-selected 8 nm (left side) and 1.8 nm (right side) NPs deposited at substrate bias voltages of 0 V (a–b), 300 V (c–d), and 1000 V (e–f). The micrographs indicate an increase in deposited material and distinct morphological changes with rising substrate bias voltage. Micrographs were captured near the NP beam center to highlight the region of maximum NP loading.

well as copper oxide bonds [32,33]. For the 8 nm NP samples, an increase of copper oxide content with substrate bias voltage is clearly visible. The 1.8 nm NP samples showed higher organic compound contributions alongside copper oxide, and no clear trend in copper oxide levels with bias voltage was observable. It has to be noted that organic compounds and possible contributions from SiO_2 cannot be discriminated due to their similar peak positions. However, based on the survey scans as well as the negligible high-resolution Si signal, peaks at higher binding energies are likely tied to organic compounds. Detailed investigations on the NP oxidation behavior are not within the scope of this manuscript and were already performed by other authors [34,35].

Quantitative XPS analysis revealed a gradual decrease in Cu content (representative of NP loading of the Si substrate surface) with increased distance from the beam center, shown in Fig. 5d. This is consistent with SEM observations and a prior study [13]. Additionally, also here the Cu content demonstrates a positive correlation over the whole distance from the beam center with substrate bias voltage, with Cu loading in size-selected 8 nm depositions rising from 26 at% to 32 at% at the beam center. A similar pattern was observed for the 1.8 nm samples. Notably, the lateral spread of NPs remained consistent across varying substrate bias voltages, suggesting that the electric field does not significantly influence the lateral distribution of NP deposition. Carbon contamination was present, accounting for 20 to 35 at% of the surface composition for 8 nm and 1.8 nm NPs, respectively. Silicon and oxygen levels rose with distance from the beam center, with silicon showing an increment from 15 at% to 20 at% for the 8 nm NPs, and from 5 at% to 20 at% for the 1.8 nm NPs. Oxygen displayed a similar pattern, increasing from about 25 at% to 40 at% some 20 mm away from the beam center. In summary, the XPS results corroborate the trends observed in the in-situ QMS data, with a higher Cu NP loading for 8 nm depositions compared to 1.8 nm NPs, albeit the difference is small. However, the increase in Cu loading with rising substrate bias voltage is clearly evident, while the lateral NP distribution remains unaffected by the substrate bias voltage.

3.4. Surface chemistry

LEIS offers even greater surface sensitivity than XPS, owing to its reliance on the scattering of low-energy ions, which probes only the outermost atomic layer [36]. This technique provides insights from the surface with minimal penetration depth, with representative 3 keV He^+ LEIS spectra depicted in Fig. 6a, which predominantly reveal Cu and O on the sample surface, alongside a minor Si presence. A gentle sputter cleaning using Ar ions, conducted before measurements within the vacuum chamber, effectively removed organic contaminants from the surface, as evidenced by the absence of a C signal and the low background noise.

Fig. 6b illustrates an increase in the Cu signal as the substrate bias voltage rises, with all spectra captured at an intermediate distance of 10 mm from the NP beam center. Spatially resolved LEIS measurements confirmed a decrease in the Cu signal with increasing distance from the NP beam center. LEIS data does not allow to distinguish between the oxidation states of Cu [36], or assign the detected oxygen to either the

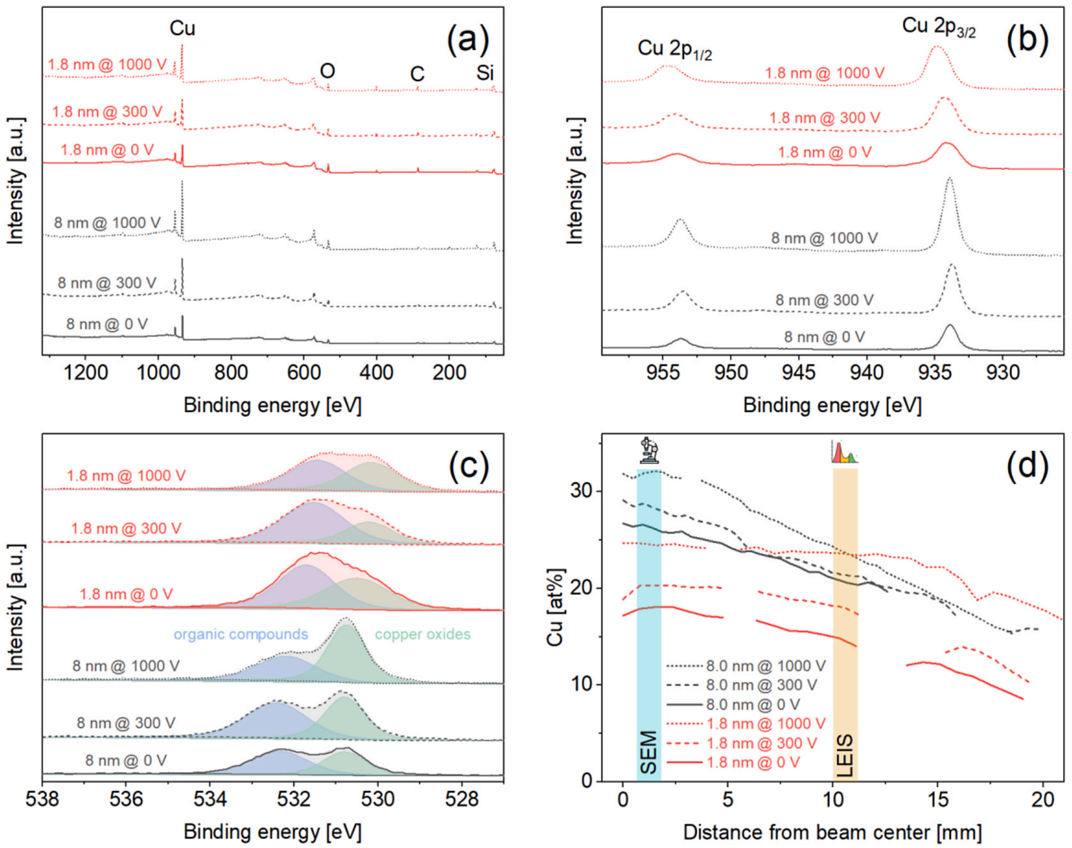

Fig. 5. Results from XPS analysis comparing thin films of size-selected 8 nm (black) and 1.8 nm (red) NPs deposited on Si substrates, showing the influence of substrate bias voltage on chemical composition and distribution. (a) XPS survey spectra highlighting the presence of elemental peaks for Cu, O, C, and Si. (b) High-resolution Cu spectra, showing an increase in Cu content with increasing substrate bias voltage. (c) High resolution O spectra, revealing contributions from organic compounds and copper oxides. (d) Quantitative analysis of Cu loading (in at%) plotted against the distance from the center of nanoparticle beam, illustrating the spatial distribution of NPs on the substrate. Approximate positions of SEM micrographs and LEIS measurements are indicated by the shaded regions. Data points overlapping with sample clamps were omitted to avoid skewed results.

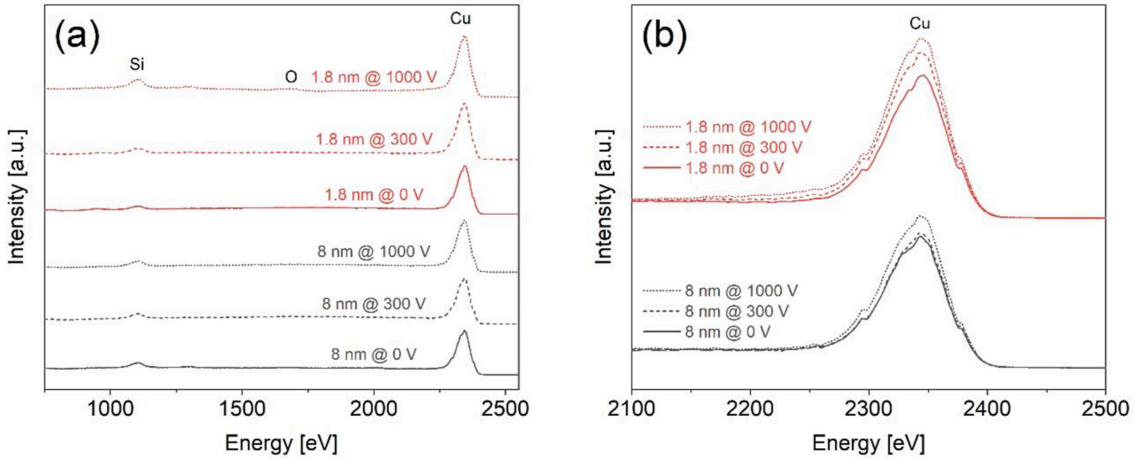

Fig. 6. Results from LEIS analysis comparing thin films of size-selected 8 nm (black) and 1.8 nm (red) NPs deposited on Si substrates, showing the influence of substrate bias voltage on chemical composition of the top atomic layer. (a) LEIS 3 keV He^+ spectra highlighting the presence of elemental peaks for Cu, O, and Si. (b) Cu spectra, showing an increased Cu signal with increasing substrate bias voltage.

copper oxide or SiO_2.

LEIS provided a stronger Cu signal for 1.8 nm samples than for 8 nm samples at the same substrate bias voltage. This is not the case for XPS, implying that the greater number of small Cu NPs are capable of achieving a greater surface coverage compared to the lower number of large 8 nm NPs. Thus, in summary, LEIS not only corroborates the XPS findings but also underscores the ability to enhance surface coverage — and consequently, the NP deposition rate — with increased substrate bias voltage.

Conducting a quantitative analysis of thin NP deposits, especially those with a thickness below 10 nm, presents notable challenges. XPS encounters its own limitations with an informational depth capped at approximately 10 nm. From comparison and agreement between our XPS and LEIS data, we can conclude that our Cu NP deposits are equal or thicker than 10 nm in the center of the NP beam. This is in good agreement with the findings derived by FIB cross-sectional analysis.

3.5. *Enhanced nanoparticle source efficiency*

The observed increase in the QMS grid current signal as a function of the substrate bias voltage suggests a rise in NP flux. To confirm that this signal indeed represents a true increase in NP yield and is not an artifact of the measurement process, we undertook a validation exercise.

One could argue that the applied substrate bias voltage affects the electric circuit of the quadrupole mass spectrometer grid, where small currents in the range of nA are measured. However, this is unlikely as the quadrupole mass spectrometer grid operates on a battery-powered circuit, ensuring it remains isolated and independent from the deposition system's power supply. Furthermore, one could speculate that the applied substrate bias voltage affects the plasma present within the deposition chamber, therefore affecting the QMS grid current signal due to the detection of plasma-derived charged species. Such a substrate bias voltage, in particular if pulsed, would certainly affect the plasma properties. However, in the case of MS-IGC, the plasma is confined within the aggregation zone. If any plasma-derived charged species, such as electrons or charged Ar ions, were to leave the aggregation chamber and reach the expansion zone containing the quadrupole mass spectrometer, they would be ejected within the quadrupole field due to their incorrect mass-to-charge ratio, thus not affecting the detected QMS grid current signal.

The presence of a plasma within the deposition chamber renders the QMS grid current signal useless due to charged species arriving at the grid. This was confirmed by performing a co-deposition of NPs along with conventional cobalt sputtering using the planar 50.8 mm magnetron sputter target located within the main deposition chamber [13]. Once the conventional sputter process commences within the deposition chamber, the QMS grid current signal becomes non-viable.

Curda et al. simulated an electrostatic field within a MS-IGC deposition chamber under comparable conditions using a potential of ±100 V, proving that NPs are affected in a distance of few cm [37]. This suggests that the provided substrate bias voltage is of sufficient strength to affect NPs traversing through the quadrupole and possibly even within the aggregation chamber. However, the latter is less likely, as the aggregation chamber is grounded and the orifice has an opening of only 3 mm.

The reason for the increased NP deposition cannot clearly be pinpointed as of now. We suggest that it is not associated with a higher NP production rate, but rather with reduced losses. This could be associated either with an increased ratio of NPs leaving the aggregation chamber rather than being lost to the chamber walls, or a reduced filtering resolution of the quadrupole mass spectrometer, with the latter as the more likely reason.

The QMS records in-situ the entire NP flux passing from the NP source into the main chamber. Only a fraction of these recorded NPs land on different positions of the substrate holder for subsequent analysis. The application of a substrate bias voltage clearly enhanced the QMS grid signal, a direct measure of the amount of extracted NPs. Within the tested range, the maximum increase was recorded at 32 % for the case of 8 nm samples. However, no general statements can be made, as the increase is likely to depend on various synthesis parameters and appears to be NP-size-dependent. Furthermore, MS-IGC suffers from a low repeatability. The phenomenon of enhanced NP flux was reversible, with the magnitude of the observed effect substantially exceeding the well-known decrease in deposition rate over time (see Fig. 3b) due to erosion-induced race track formation on the target [17] and a decrease in oxygen impurities in our system's aggregation chamber [10].

The notion of an improved NP efficiency of the NP source is in contrast to the well-established fundamentals of thin film growth on biased substrates [38], which lead to a densification of the film morphology and to reduced growth rates due to re-sputtering effects. In MS-IGC in conjunction with QMS, such an electric field is unlikely to significantly change the sputter conditions around the sputter target due to the de-coupled nature of the individual highly functionalized process chambers.

3.6. *Discussion on nanoparticle thin film formation mechanisms*

Increasing the kinetic energies of single-charged NPs by 300 eV and 1000 eV constitutes a considerable addition to the NPs' total energy, significantly influencing the NP-surface interaction. In literature, three principal deposition regimes, namely soft landing, pinning, and implantation, are distinguished by their respective kinetic energy per atom [23].

This is particularly relevant when considering the vast difference in atom numbers between small (approximately 260 atoms for spherical 1.8 nm NPs) and large NPs (about 23,000 atoms for 8 nm NPs). With an assumed speed of 100 m s^{-1} [39] and thus a kinetic energy below 0.01 eV atom^{-1} for non-accelerated NPs, the application of a 1000 V substrate bias voltage to 1.8 nm negatively charged NPs results in an energy of approximately 4 eV atom^{-1}, surpassing the threshold for soft landing [23] and reaching beyond the intermediate pinning regime into the implantation regime, as the binding energy of small Cu clusters can be expected to be in the range of 2 eV atom^{-1} [40]. The chosen range of substrate bias voltages in this work thus provides a comprehensive spectrum of NP landing conditions.

In his early work, Haberland et al. already applied a positive substrate bias voltage to accelerate metallic NPs towards the substrate, resulting in the formation of highly reflective and strongly adhering Mo NP films on polished Cu substrates [8,19]. Size-selected Ag NPs were studied by Shyjumon et al. under substrate bias voltages ranging from −500 to −2500 V to attract positively charged NPs, noting an increasing flattening of NPs with increasing kinetic energy [21]. These findings are in line with our own, where we noted a densification in the thin film's structure corresponding with an increase in substrate bias voltage. The underlying mechanism can be attributed to the high-velocity impacts (e.g., single-charged 1.8 nm NPs with a kinetic energy of 1000 eV at a 1000 V bias voltage reach speeds of 3500 m s^{-1}), which create localized high-temperature spots upon each NP's impact [19]. In the case of the non-accelerated NPs forming thin films, only negligible NP deformation is expected for both small and large NPs [23]. With rising impact energy, increased flattening and plastic deformation is expected. In the case of 8 nm NP samples deposited at 1000 V, despite a low total impact energy of around 0.05 eV atom^{-1}, this still represents an increase of more than 1000 % in impact energy compared to the non-accelerated deposition, with an impact velocity of ~400 m s^{-1}, thus explaining the observed changes in the morphology as a function of the substrate bias voltage.

Regarding morphological changes, Rattunde et al. [20] reported two opposing effects related to the application of a substrate bias voltage up to 30 kV to Cu NPs: For initially rough substrate surfaces, a smoothening is observed, while impinging NPs logarithmically increase the roughness of an initially smooth surface. Michelakaki et al. [22] demonstrated that by adjusting the substrate bias voltage to alter the kinetic energy of Hf NPs, one can produce porous thin films, whose mechanical properties increasingly resemble those of conventionally sputtered ones as the substrate bias voltage rises. This mechanical similarity to dense sputtered films is in agreement with our observations of increased density with increasing bias voltage.

4. Conclusions

In this study, we have demonstrated that the application of a substrate bias voltage can significantly increase the deposition rate of size-selected nanoparticles by magnetron sputter inert gas condensation coupled with quadrupole mass spectrometry. This enhanced nanoparticle yield was monitored in-situ for different nanoparticle sizes and subsequently verified through scanning electron microscopy, X-ray photoelectron spectroscopy, and low-energy ion scattering spectroscopy. Our results indicate a significant enhancement of up to 32 % in the nanoparticle deposition rate with a distinct evolution in surface morphology, illustrating the beneficial impact of the kinetic energy on film characteristics. The advancements in process efficiency detailed in this work mark a step forward in the optimization of magnetron sputter inert gas condensation for industrial applications.

CRediT authorship contribution statement

Florian Knabl: Writing – original draft, Visualization, Investigation, Formal analysis, Conceptualization. **Dominik Gutnik:** Writing – review & editing, Visualization, Investigation, Formal analysis, Conceptualization. **Prathamesh Patil:** Writing – review & editing, Visualization, Investigation, Formal analysis, Conceptualization. **Christine Bandl:** Writing – review & editing, Investigation, Formal analysis. **Tijmen Vermeij:** Writing – review & editing, Investigation, Formal analysis. **Christian M. Pichler:** Writing – review & editing, Supervision, Conceptualization. **Barbara Putz:** Writing – review & editing, Supervision, Conceptualization. **Christian Mitterer:** Writing – review & editing, Supervision, Conceptualization.

Declaration of competing interest

The authors declare that they have no known competing financial interests or personal relationships that could have appeared to influence the work reported in this paper.

Acknowledgements

Funding support by the Austrian Research Promotion Agency (FFG, Project Nr. 896659 AMAGADE) and Gesellschaft für Forschungsförderung Niederösterreich (Project FTI21-D002) is gratefully acknowledged. B.P. acknowledges funding from the Swiss National Science Foundation under the Ambizione grant agreement No PZ00P2_202089.

Data availability

Data will be made available on request.

References

[1] Y. Zhou, C. Jin, Y. Li, W. Shen, Dynamic behavior of metal nanoparticles for catalysis, Nano Today 20 (2018) 101–120, https://doi.org/10.1016/j.nantod.2018.04.005.

[2] Y.J. Lin, S.J. Ding, K. Chen, D.J. Yang, Y. Xie, Z.H. Hao, L. Zhou, Q.Q. Wang, Plasmon-enhanced photocatalytic activity of Pt@Au and Pt@Cu nanoparticles in quantum size regime, J. Nanoparticle Res. 21 (2019) 137, https://doi.org/10.1007/s11051-019-4581-7.

[3] S. Haviar, J. Čapek, Š. Batková, N. Kumar, F. Dvořák, T. Duchoň, M. Fialová, P. Zeman, Hydrogen gas sensing properties of WO_3 sputter-deposited thin films enhanced by on-top deposited CuO nanoclusters, Int. J. Hydrogen Energy 43 (2018) 22756–22764, https://doi.org/10.1016/J.IJHYDENE.2018.10.127.

[4] N. Kostoglou, C.W. Liao, C.Y. Wang, J.N. Kondo, C. Tampaxis, T. Steriotis, K. Giannakopoulos, A.G. Kontos, S. Hinder, M. Baker, E. Bousser, A. Matthews, C. Rebholz, C. Mitterer, Effect of Pt nanoparticle decoration on the H_2 storage performance of plasma-derived nanoporous graphene, Carbon 171 (2021) 294–305, https://doi.org/10.1016/j.carbon.2020.08.061.

[5] M. Vaidulych, A. Shelemin, J. Hanuš, I. Khalakhan, I. Krakovsky, P. Kočová, H. Mašková, J. Kratochvíl, P. Pleskunov, J. Štěrba, O. Kylián, A. Choukourov, H. Biederman, Superwettable antibacterial textiles for versatile oil/water separation, Plasma Process. Polym. 16 (2019) 1900003, https://doi.org/10.1002/ppap.201900003.

[6] N. Khomiakova, D. Nikitin, A. Kuzminova, M. Cieslar, Y. Al-Muhkhrabi, D. Kahoun, J. Lieskovská, J. Hanuš, J. Kratochvíl, P. Pleskunov, J. Vyskočil, A. Choukourov, O. Kylián, H. Biederman, Cu/Ag bimetallic nanoparticles produced by cylindrical post-magnetron gas aggregation source – a novel galvanic corrosion-based antibacterial material, Vacuum 217 (2023) 112586, https://doi.org/10.1016/j.vacuum.2023.112586.

[7] T. Patlejchová, E. Kratochvílová, H. Mašková, D. Kahoun, O. Kylián, Y. Al-Muhkhrabi, O. Mashchenko, J. Štěrba, J. Kratochvíl, Galvanic corrosion of copper induced by metal nanoparticles for creating antiviral nanocomposites, ACS Appl. Nano Mater. 6 (2023) 23090, https://doi.org/10.1021/acsanm.3c04447.

[8] H. Haberland, M. Karrais, M. Mall, A new type of cluster and cluster ion source, Z. Physik D Atoms, Mol. Clust. 20 (1991) 413–415, https://doi.org/10.1007/BF01544025.

[9] O. Polonskyi, P. Solař, O. Kylián, M. Drábik, A. Artemenko, J. Kousal, J. Hanuš, J. Pešička, I. Matolínová, E. Kolíbalová, D. Slavínská, H. Biederman, Nanocomposite metal/plasma polymer films prepared by means of gas aggregation cluster source, Thin Solid Films 520 (2012) 4155–4162, https://doi.org/10.1016/j.tsf.2011.04.100.

[10] O. Polonskyi, O. Kylián, M. Drábik, J. Kousal, P. Solař, A. Artemenko, J. Čechvala, A. Choukourov, D. Slavínská, H. Biederman, Deposition of Al nanoparticles and their nanocomposites using a gas aggregation cluster source, J. Mater. Sci. 49 (2014) 3352–3360, https://doi.org/10.1007/s10853-014-8042-5.

[11] M. Ganeva, T. Peter, S. Bornholdt, H. Kersten, T. Strunskus, V. Zaporojtchenko, F. Faupel, R. Hippler, Mass spectrometric investigations of nano-size cluster ions produced by high pressure magnetron sputtering, Contrib. Plasma Phys. 52 (2012) 881–889, https://doi.org/10.1002/CTPP.201200046.

[12] V.N. Popok, L. Gurevich, Charge states of size-selected silver nanoparticles produced by magnetron sputtering, J. Nanoparticle Res. 21 (2019) 171, https://doi.org/10.1007/s11051-019-4615-1.

[13] F. Knabl, C. Bandl, T. Griesser, C. Mitterer, In situ and ex situ quantification of nanoparticle fluxes in magnetron sputter inert gas condensation: a Cu nanoparticle case study, J. Vac. Sci. Technol. A 42 (2024) 023201, https://doi.org/10.1116/6.0003283.

[14] Y. Huttel, L. Martínez, A. Mayoral, I. Fernández, Gas-phase synthesis of nanoparticles: present status and perspectives, MRS Commun 8 (2018) 947–954, https://doi.org/10.1557/mrc.2018.169.

[15] A. Marek, J. Valter, S. Kadlec, J. Vyskočil, Gas aggregation nanocluster source — reactive sputter deposition of copper and titanium nanoclusters, Surf. Coat. Technol. 205 (2011) S573–S576, https://doi.org/10.1016/j.surfcoat.2010.12.027.

[16] G. Krishnan, S. de Graaf, G.H. ten Brink, P.O.Å. Persson, B.J. Kooi, G. Palasantzas, Strategies to initiate and control the nucleation behavior of bimetallic nanoparticles, Nanoscale 9 (2017) 8149–8156, https://doi.org/10.1039/C7NR00916J.

[17] M. Ganeva, A.V. Pipa, R. Hippler, The influence of target erosion on the mass spectra of clusters formed in the planar DC magnetron sputtering source, Surf. Coat. Technol. 213 (2012) 41–47, https://doi.org/10.1016/j.surfcoat.2012.10.012.

[18] S. Ali-Ogly, J. Kousal, D. Nikitin, P. Pleskunov, J. Hanuš, A. Choukourov, H. Biederman, Computational fluid dynamics predicts the nanoparticle transport in gas aggregation cluster sources, J. Phys. D Appl. Phys. 55 (2022) 12, https://doi.org/10.1088/1361-6463/ac8c4e.

[19] H. Haberland, M. Karrais, M. Mall, Y. Thurner, Thin films from energetic cluster impact: a feasibility study, J. Vac. Sci. Technol. A 10 (1992) 3266–3271, https://doi.org/10.1116/1.577853.

[20] O. Rattunde, M. Moseler, A. Häfele, J. Kraft, D. Rieser, H. Haberland, Surface smoothing by energetic cluster impact, J. Appl. Phys. 90 (2001) 3226–3231, https://doi.org/10.1063/1.1398067.

[21] I. Shyjumon, M. Gopinadhan, O. Ivanova, M. Quaas, H. Wulff, C.A. Helm, R. Hippler, Structural deformation, melting point and lattice parameter studies of size selected silver clusters, Eur. Phys. J. D 37 (2006) 409–415, https://doi.org/10.1140/epjd/e2005-00319-x.

[22] I. Michelakaki, N. Boukos, D.A. Dragatogiannis, S. Stathopoulos, C.A. Charitidis, D. Tsoukalas, Synthesis of hafnium nanoparticles and hafnium nanoparticle films by gas condensation and energetic deposition, Beilstein J. Nanotechnol. 9 (2018) 1868–1880, https://doi.org/10.3762/bjnano.9.179.

[23] V.N. Popok, I. Barke, E.E.B. Campbell, K.H. Meiwes-Broer, Cluster–surface interaction: from soft landing to implantation, Surf. Sci. Rep. 66 (2011) 347–377, https://doi.org/10.1016/j.surfrep.2011.05.002.

[24] G. Greczynski, L. Hultman, X-ray photoelectron spectroscopy: towards reliable binding energy referencing, Prog. Mater. Sci. 107 (2020) 100591, https://doi.org/10.1016/j.pmatsci.2019.100591.

[25] G. Greczynski, L. Hultman, Reliable determination of chemical state in x-ray photoelectron spectroscopy based on sample-work-function referencing to adventitious carbon: resolving the myth of apparent constant binding energy of the C 1s peak, Appl. Surf. Sci. 451 (2018) 99–103, https://doi.org/10.1016/j.apsusc.2018.04.226.

[26] G. Greczynski, R.T. Haasch, N. Hellgren, E. Lewin, L. Hultman, X-ray photoelectron spectroscopy of thin films, Nat. Rev. Methods Prim. 3 (2023) 40, https://doi.org/10.1038/s43586-023-00225-y.

[27] G. Greczynski, L. Hultman, C 1s peak of adventitious carbon aligns to the vacuum level: dire consequences for material's bonding assignment by photoelectron spectroscopy, ChemPhysChem 18 (2017) 1507–1512, https://doi.org/10.1002/CPHC.201700126.

[28] G.E. Johnson, R. Colby, J. Laskin, Soft landing of bare nanoparticles with controlled size, composition, and morphology, Nanoscale 7 (2015) 3491–3503, https://doi.org/10.1039/c4nr06758d.

[29] W. Chamorro-Coral, A. Caillard, P. Brault, P. Andreazza, C. Coutanceau, S. Baranton, The role of oxygen on the growth of palladium clusters synthesized by gas aggregation source, Plasma Process. Polym. 16 (2019) e1900006, https://doi.org/10.1002/ppap.201900006.

[30] A. Kusior, K. Kollbek, K. Kowalski, M. Borysiewicz, T. Wojciechowski, A. Adamczyk, A. Trenczek-Zajac, M. Radecka, K. Zakrzewska, Sn and Cu oxide

nanoparticles deposited on TiO_2 nanoflower 3D substrates by Inert Gas Condensation technique, Appl. Surf. Sci. 380 (2016) 193–202, https://doi.org/10.1016/j.apsusc.2016.01.204.

[31] J.A. Torres-Ochoa, D. Cabrera-German, O. Cortazar-Martinez, M. Bravo-Sanchez, G. Gomez-Sosa, A. Herrera-Gomez, Peak-fitting of Cu 2p photoemission spectra in Cu^0, Cu^{1+}, and Cu^{2+} oxides: a method for discriminating Cu^0 from Cu^{1+}, Appl. Surf. Sci. 622 (2023) 156960 https://doi.org/10.1016/j.apsusc.2023.156960.

[32] Thermo Fisher Scientific Inc, Oxygen X-ray photoelectron spectra, oxygen electron configuration, and other elemental information, n.d. https://www.thermofisher.com/at/en/home/materials-science/learning-center/periodic-table/non-metal/oxygen.html. (Accessed 9 March 2024).

[33] S. Poulston, P.M. Parlett, P. Stone, M. Bowker, Surface oxidation and reduction of CuO and Cu_2O studied using XPS and XAES, Surf. Interface Anal. 24 (1996) 811–820, https://doi.org/10.1002/(SICI)1096-9918(199611)24:12<811::AID-SIA191>3.0.CO;2-Z.

[34] V.N. Popok, S.M. Novikov, Y.Y. Lebedinskij, A.M. Markeev, A.A. Andreev, I. N. Trunkin, A. V Arsenin, V.S. Volkov, Gas-aggregated copper nanoparticles with long-term plasmon resonance stability, Plasmonics 16 (2021) 333–340, https://doi.org/10.1007/s11468-020-01287-4.

[35] F. Zamboni, A. Makarevičiūtė, V.N. Popok, Long-Term plasmonic stability of copper nanoparticles produced by gas-phase aggregation method followed by UV-ozone treatment, Appl. Nanosci. 3 (2022) 102–111, https://doi.org/10.3390/applnano3020007.

[36] C. V Cushman, P. Brüner, J. Zakel, G.H. Major, B.M. Lunt, N.J. Smith, T. Grehl, M. R. Linford, Low energy ion scattering (LEIS). A practical introduction to its theory, instrumentation, and applications, Anal. Methods 8 (2016) 3419–3439, https://doi.org/10.1039/C6AY00765A.

[37] P. Curda, D. Kaftan, T. Kozak, S. Kumar, P. Sezemský, V. Stranak, High-defined and size-selective deposition of nanoparticles by their manipulation in an electrostatic field, Appl. Surf. Sci. 640 (2023) 158307, https://doi.org/10.1016/j.apsusc.2023.158307.

[38] I. Petrov, P.B. Barna, L. Hultman, J.E. Greene, Microstructural evolution during film growth, J. Vac. Sci. Technol. A 21 (2003) S117–S128, https://doi.org/10.1116/1.1601610.

[39] P. Solař, K. Škorvánková, A. Kuzminova, J. Kousal, O. Kylián, Measurement of velocities of copper nanoparticles exiting a gas aggregation source, Vacuum 202 (2022) 111114, https://doi.org/10.1016/J.VACUUM.2022.111114.

[40] Y.D. Qu, X.L. Liang, X.Q. Kong, W.J. Zhang, Size-dependent cohesive energy, melting temperature, and Debye temperature of spherical metallic nanoparticles, Phys. Met. Metallogr. 118 (2017) 528–534, https://doi.org/10.1134/S0031918X17060102.